Global observations of ring current dynamics during corotating interaction region–driven geomagnetic storms in 2008

E. W. Grimes,[1] J. D. Perez,[1] J. Goldstein,[2,3] D. J. McComas,[2,3] and P. Valek[2,3]

[1]   We examine the evolution of the ring current during the main and early recovery phases of three geomagnetic storms driven by corotating interaction regions. The equatorial energy density profiles of 5–30 keV ions are calculated from deconvolved energetic neutral atom images from the Two Wide-Angle Imaging Neutral-Atom Spectrometers mission. The energy density in the ring current is enhanced by almost a factor of 2 and stretches from postmidnight to dusk immediately following injections identified by in situ measurements. The energy density then drops back to preinjection levels within 1–2 h. We also find that there are often two peaks in the energy density following the injection, one at midnight and one close to dusk. We present the spectra for these peaks to show they contain different ion populations. The asymmetry of the ring current observed is found to agree with previous in situ and simulation studies.

1. Introduction

[2]   Geomagnetic storms during the declining phase of the solar cycle are predominantly driven by corotating interaction regions (CIRs) originating at coronal holes on the Sun [*Krieger et al.*, 1973; *Tsurutani et al.*, 2006]. Because of the different driving mechanisms in the solar wind, these storms are inherently different than their interplanetary coronal mass ejection (ICME) counterparts. CIRs produce weak storms with recovery phases that typically last from several days to several weeks. These long recovery phases are due to non-linear Alfven waves that follow the fast stream interface [*Tsurutani and Gonzalez*, 1987]. Protons are injected into the magnetosphere by these Alfven waves when the oscillating B_z component of the interplanetary magnetic field (IMF) becomes negative [*Sandanger et al.*, 2005]. *Tsurutani et al.* [2006] found a one-to-one relationship between southward IMF B_z, decreases in Dst, and AE increases during the recovery phase of a CIR storm, suggesting that the ring current is directly influenced by the interplanetary Alfven waves through High-Intensity Long-Duration Continuous AE Activity (HILDCAA) events. *Denton et al.* [2006] and *Borovsky and Denton* [2006] use a superposed epoch analysis to study the different responses of the magnetosphere to these different drivers. Most notably, they find that geomagnetic storms driven by CIRs have a less dense, but hotter plasma sheet than that of ICMEs.

[3]   The peak in ring current pressure is thought to reside in the dusk-midnight region. For example, *Stüdemann et al.* [1987] found that protons with energies up to ~140 keV are significantly enhanced in the dusk region as compared to dawn using in situ data from a few hours after onset of a geomagnetic storm. Using a statistical analysis of in situ measurements from ISEE, AMPTE/CCE, and Polar, *Le et al.* [2004] and *Lui* [2003] also found the same local time asymmetry with higher plasma pressures in the dusk-midnight region. *Korth et al.* [1999], *Denton et al.* [2005], and *Zhang et al.* [2006] all used data from the magnetospheric plasma analyzer (MPA) instrument onboard LANL geosynchronous satellites to show this local time asymmetry also exists in proton density and temperature at geosynchronous orbit. *Zhang et al.* [2007] also observed an asymmetrical ring current using simulations of plasma pressure during a moderate storm. Linear inversions of energetic neutral atom (ENA) observations by *Brandt et al.* [2002], however, showed a peak in plasma pressure in the postmidnight region. The authors suggested that this effect could be due to shielding electric field created in the ring current or by a skewed convection pattern due to IMF B_y. *Ebihara and Fok* [2004] used the Comprehensive Ring Current Model (CRCM) to show that this postmidnight peak in plasma pressure could be due to a deformation of the convection electric field due to shielding and/or due to the local time dependence of the plasma sheet density, as well as a skewed convection pattern due to IMF B_y. More recently, *Buzulukova et al.* [2010] used CRCM to verify that overall convection strength and electric field skewing due to shielding are the most important factors behind postmidnight enhancements.

[4]   *Iyemori and Rao* [1996] found that the recovery of Sym-H is accelerated just after substorm onset during the

[1]Physics Department, Auburn University, Auburn, Alabama, USA.
[2]Southwest Research Institute, San Antonio, Texas, USA.
[3]University of Texas, San Antonio, Texas, USA.
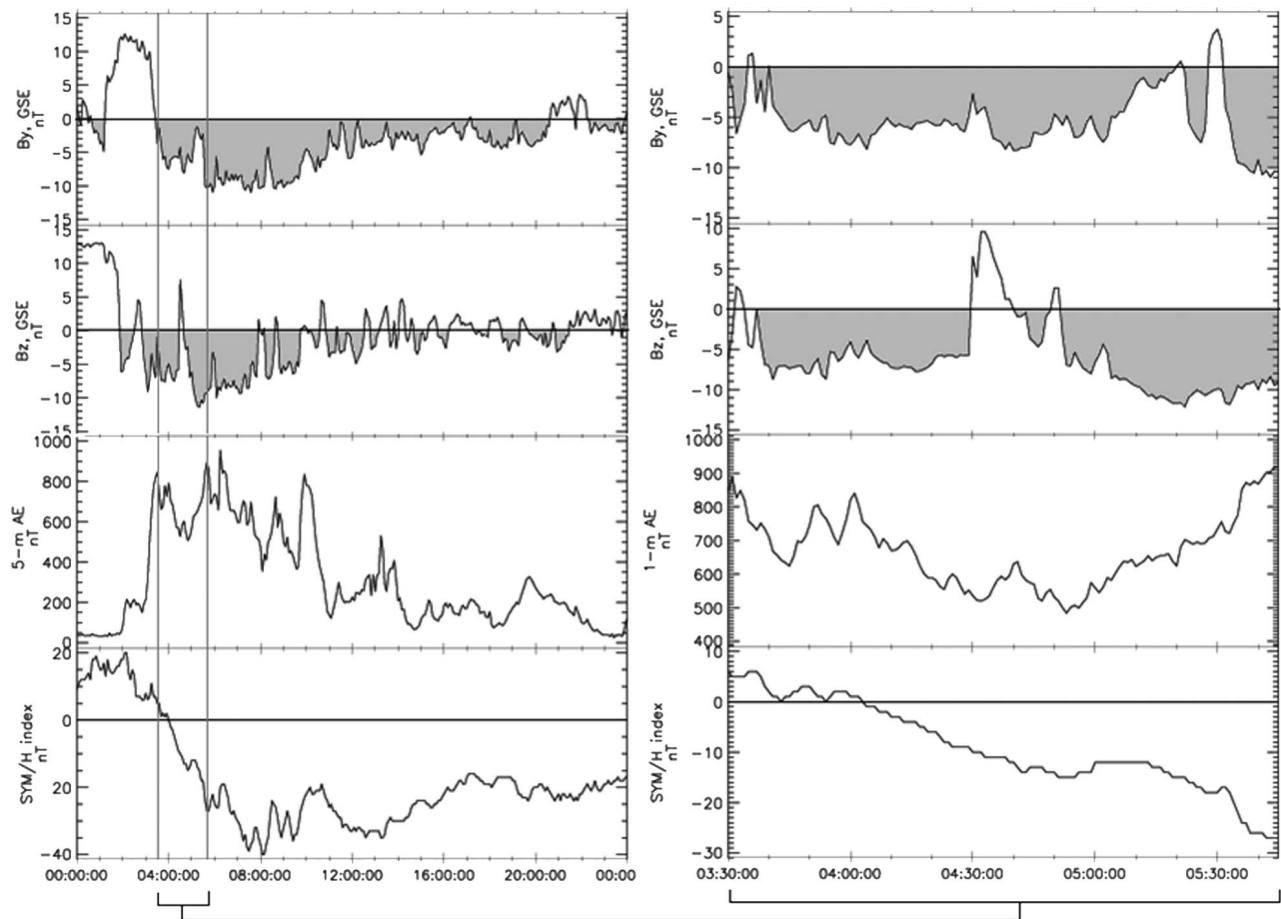
**Figure 1.** The IMF B_y, B_z, AE, and Sym-H indices for (left) 12 July 2008 and (right) 0330 UT-0545 UT.

recovery phase of storms. This is counterintuitive, as the substorm should inject fresh plasma into the ring current, which should lead to a more intense ring current and decrease Sym-H. Both *Lui et al.* [2001] and *Ohtani et al.* [2005] showed that ring current ENA intensity increases after substorm onset, which is evidence of fresh plasma being injected. *Siscoe and Petschek* [1997] suggested that the increase in Sym-H is due to the reduction of the cross-tail current just after substorm onset. *Ohtani et al.* [2001] used a statistical study to show that the geosynchronous magnetic field tends to dipolarize near minimum Sym-H and the subsequent recovery of Sym-H is due to the reduction of the cross-tail current, as suggested by *Siscoe and Petschek* [1997]. *Ohtani et al.* [2005] showed this same counterintuitive relationship between Sym-H and ring current strength using ENA intensities measured by the high-energy neutral atom (HENA) imager.

[5] The Two Wide-Angle Imaging Neutral-Atom Spectrometers (TWINS) mission is a mission of opportunity through the NASA Explorer program to simultaneously observe energetic neutral atoms (ENAs) created when positively charged ions charge exchange with cold neutral hydrogen (at high altitudes) and cold neutral oxygen (at low altitudes) in the magnetosphere. TWINS observes ENAs from 1 to 100 keV with a 4° × 4° degree angular resolution and completes a single sweep image in just over a minute. A

full description of the instrumentation can be found in the work of *McComas et al.* [2009a]. We focus on the viewing of ENAs produced between 5 and 30 keV from TWINS-1 using 33 min integrations (24 sweep statistically smoothed images) in this study.

[6] The statistical smoothing is a technique to ensure that each pixel contains a statistically significant number of counts [*McComas et al.*, 2009b]. The technique uses a set target value, and when a pixel contains counts less than the target value, nearby pixels are added until the target is reached. Once the target value is reached, the total number of counts is recorded in that pixel. The total geometric factor for the new area is also recorded and used in the calculation of ENA intensities, allowing for regions with higher counts to use smaller areas to reach the target value. This allows for the least amount of smoothing in areas where we observe the highest number of counts. A more extensive discussion of the statistical smoothing technique is provided by Valek et al. (ENA observations of the moderate storm of 2009, 22 July 2010).

[7] The ion intensities are extracted from the ENA images by expanding the unknown intensities in terms of tricubic B splines and solving a set of integral equations for the expansion coefficients. A set of linear equations are derived by requiring that the expansion coefficients minimize normalized chi-square, i.e., the ion distribution fits the data,
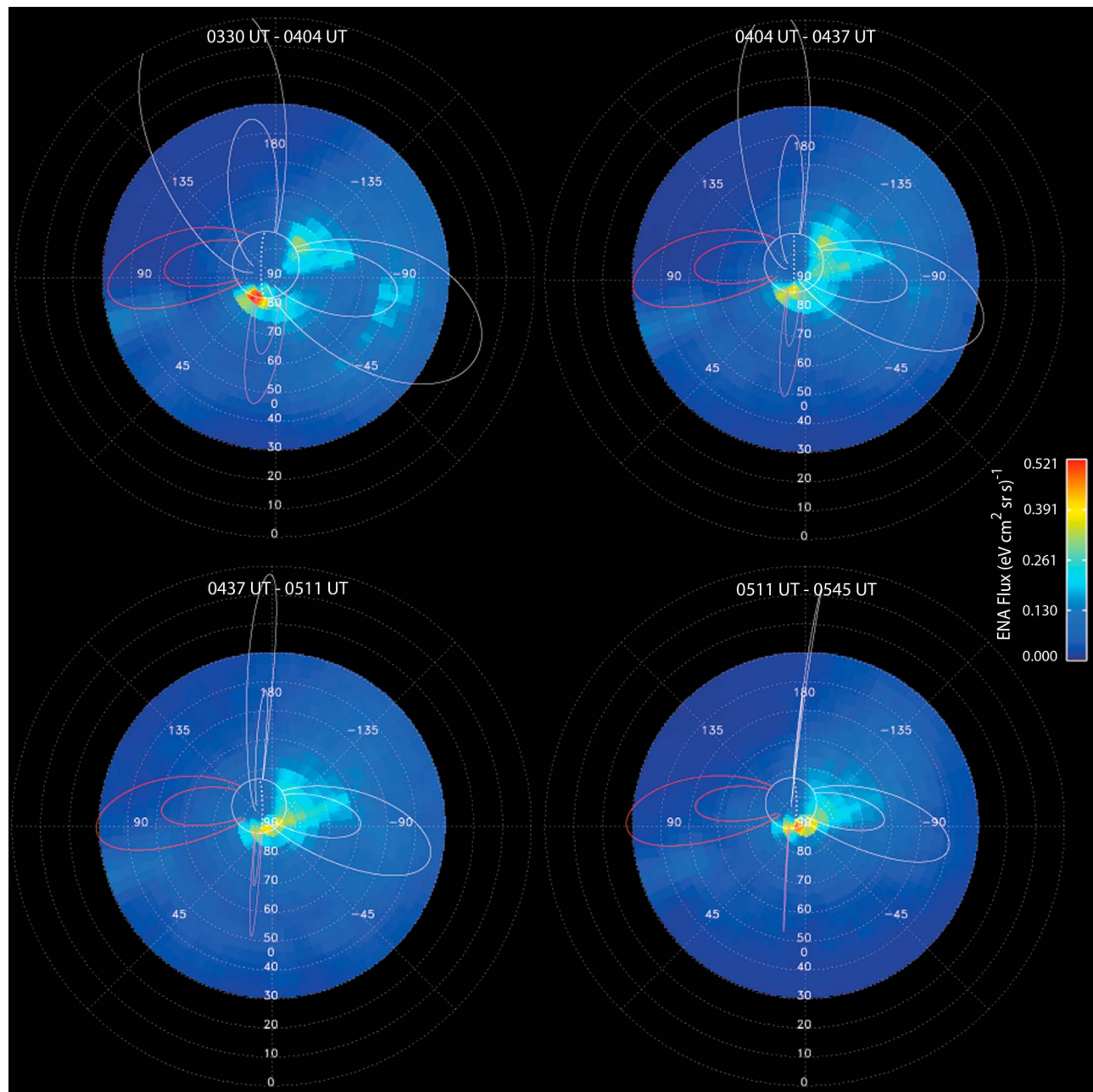
Figure 2. TWINS-1 10 keV ENA flux for 12 July, 0330–0545 UT.

and a penalty function that regularizes the equations and imposes a constraint of smoothness for the ion distribution. The penalty function is derived by *Wahba* [1990] using the formalism of reproducing kernal Hilbert spaces and the principles of Bayesian statistics. The balance between fitting the data and smoothness is determined by demanding that normalized chi-square is unity. Furthermore, positivity constraints are imposed to prevent the ion distribution from going too far negative in regions of low intensity and limited data. The details of the method are given in J. D. Perez et al. (Validation of a method for obtaining ion intensities from ENA images using data from TWINS and

THEMIS, submitted to *Journal of Geophysical Research*, 2010).

[8] In this paper, we examine the evolution of the terrestrial ring current during three CIR-driven geomagnetic storms using 5–30 keV ion intensities deconvolved from the TWINS-1 ENA imager. The first event examined is during the main phase of a storm on 12 July 2008, just prior to a dipolarization signature measured in the midnight region and subsequently near dusk by GOES magnetometers at geosynchronous orbit. The equatorial energy density for 5–30 keV ions peaks across the night side ring current in the time interval following the injection inferred by the dipolarization observed at geosynchronous orbit. At 2 h after the
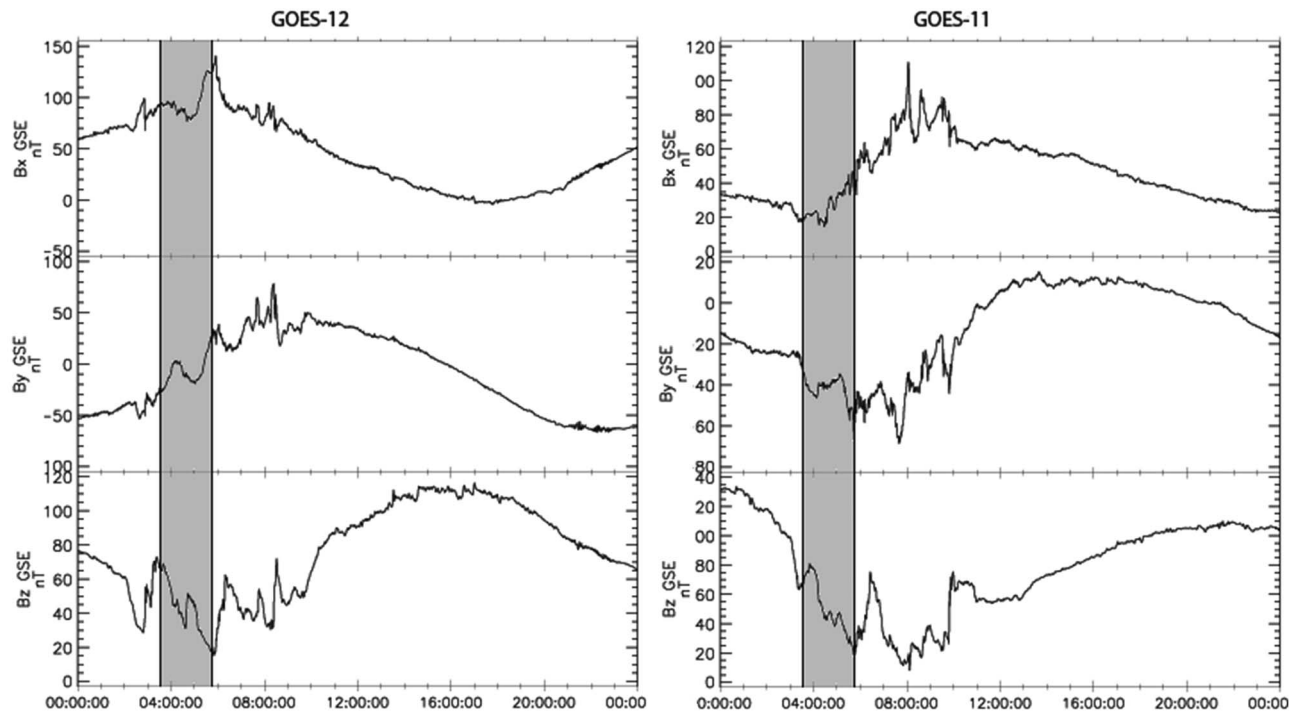
**Figure 3.** (left) GOES-12 and (right) GOES-11 geomagnetic field data for 12 July 2008.

injection, the energy density has dropped off significantly and is peaked near midnight. The ion spectra of this peak shows a Maxwellian peaked at 10 keV. The second event examined is during the early recovery phase of a storm on 10 August 2008. A dipolarization is observed by GOES-11 near dusk just before being measured by GOES-12 near midnight. The equatorial energy density increases by a factor of 2 during the time frame following the presumed injection. The third event examined, 4 September 2008, is also during the early recovery phase. Data for this event include Geotail observations of an earthward plasma injection in the plasma sheet, followed by GOES observations of a dipolarization signature near midnight. Again, the deconvolved energy density increases by a factor of 2 immediately following the injection and then decreases. In each case during the early recovery phase, we observe two peaks in the energy density after the injection, the first being at midnight and the second toward dusk.

2. Observations

[9] The geomagnetic storms presented in this section occur during three successive months and are due to a 27 day recurring CIR structure in the solar wind. The structure in the solar wind can be further identified by the Alfven waves following the stream interface which drive the oscillating B_z component of the interplanetary magnetic field. The interval of time for these events was chosen at times of highest geomagnetic activity, so as to have the highest counts into the instrument. The storms driven by this CIR structure are only small- to moderate-sized storms as defined by *Gonzalez et al.* [1994].

2.1. The 12 July 2008 Event

[10] Figure 1 shows 5 min averages of IMF B_y, B_z, the auroral electrojet index (AE), and Sym-H index provided by OMNI for the day of 12 July 2008 (Figure 1, left). The oscillatory nature of IMF B_z about zero is clear in the recovery phase late in the day. The vertical lines on the left plot indicate the time interval observed by TWINS-1, and we zoom in on this interval using 1 min OMNI data on the right. The IMF conditions are time shifted to the magnetopause by OMNI. IMF B_y is mostly negative for the entire interval, with slight positive excursions around 0335 and 0530 UT. IMF B_z is also mostly negative for this interval, with a 10 min northerly excursion at 0430 UT. The AE index is elevated for the interval, with peaks around 900 nT at 0330 and 0545 UT. Sym-H shows that the time of interest is at the beginning of the main phase of the storm and goes from positive to negative at 0400 UT, dropping to almost -30 nT for the interval.
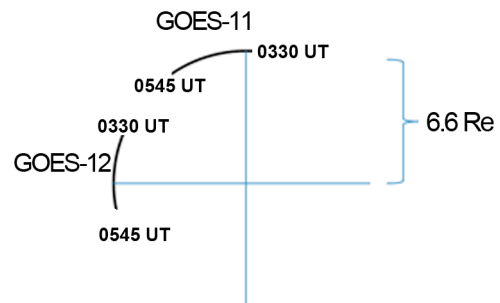
Figure 4. GOES equatorial spacecraft locations for 0330–0545 UT on 12 July 2008.
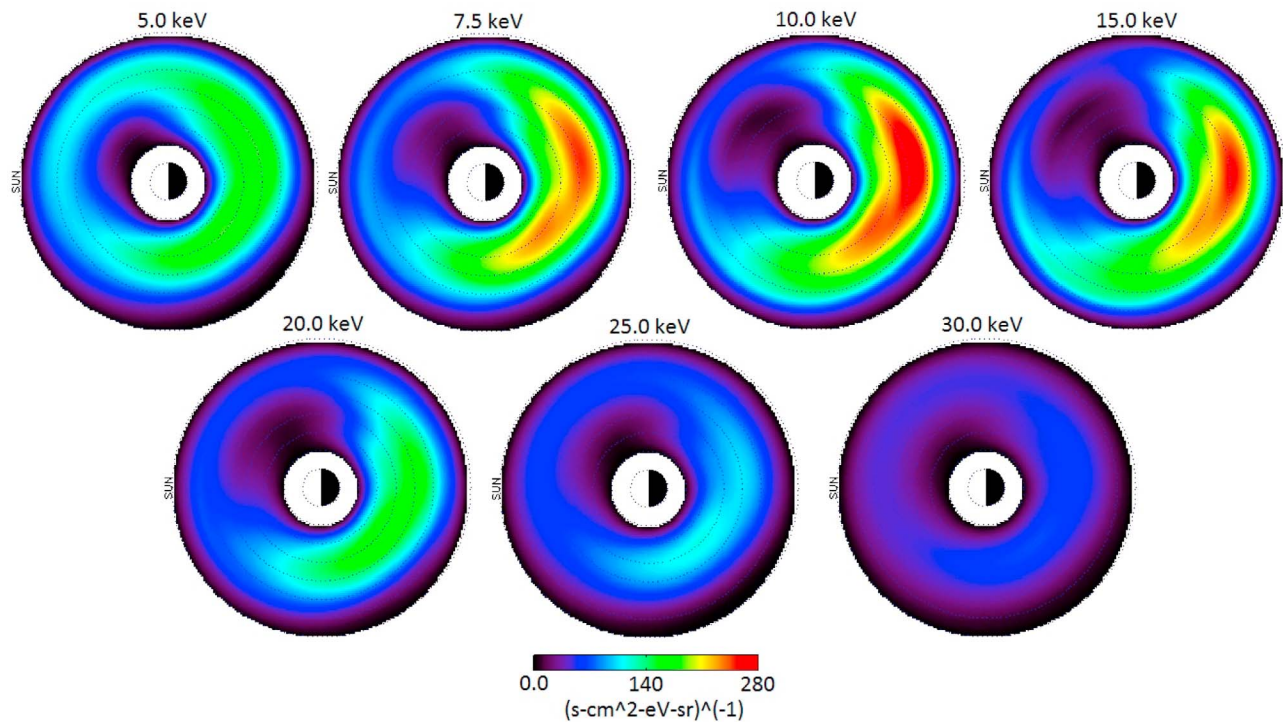
Figure 5. Equatorial intensity averaged over pitch angle for 5–30 keV ions on 12 July 2008, 0511–0545 UT.

[11] Figure 2 shows the 10 keV ENA images for 0330–0545 UT. The images are 24 sweep, 33 min averages projected onto a sky map view with dipole field lines at McIlwain L shells of $L = 4$ and $L = 8$. The red and purple L shells indicate the sunward and duskward directions, respectively. During 0330–0404 UT, the TWINS-1 spacecraft is at $R = $ ~5 R_e, 52° latitude and is viewing from postdawn in the Northern Hemisphere. Strong low-altitude emissions are observed just off the Earth's limb from both the Northern Hemisphere and Southern Hemisphere. High-altitude emissions are observed at midnight around the $L = 4$ dipole L shell. From 0404 to 0437 UT, TWINS-1 has moved to $R = 5.6$ R_e, 57° latitude. The ENAs produced at low altitude have decreased by ~25% and are still observed emanating from both hemispheres. By 0438–0511 UT, the spacecraft has moved to $R = 6.1$ R_e, 60° latitude and no longer sees the low-altitude emissions from the Southern Hemisphere. Both high-altitude and low-altitude ENAs have increased by ~10%. From 0511 to 0545 UT, the spacecraft is at $R = 6.5$ R_e, 63° latitude. Low-altitude emissions have increased by another ~15%, almost reaching the ENA flux observed during the 0330–0404 UT period.

[12] GOES-11 (right) and GOES-12 (left) magnetometer data are presented in Figure 3, with GOES equatorial positions shown in Figure 4. A dipolarization signature, a sharp increase in B_z, is measured at GOES-12 in the premidnight region just before 0300 UT. The dipolarization signature is then measured by GOES-11 near dusk at 0330 UT. A second, much smaller dipolarization signature is measured by GOES 12 close to 0445 UT. Both GOES-11 and GOES-12 continue to observe dipolarization signatures on the nightside for several hours after the interval of interest.

[13] As an example of the energy-dependent global images during this period, the deconvolved 5–30 keV equatorial ion intensities for 0511–0545 UT are presented in Figure 5. The sunward direction is to the left in all images. We observe a single peak in ion intensity at 10 keV near midnight. The peak in ion intensity at lower energies is slightly more dawnward than the peak in higher energies, consistent with gradient and curvature drift of the ions [*Ejiri et al.*, 1980; *Fok et al.*, 1996; *Kistler and Larson*, 2000], although detailed analysis of the drift dynamics is beyond the scope of this paper.

[14] In Figure 6, we present the time evolution of the spectra of the distribution at its peak intensity ($R = 5.3$ R_e, MLT = 0.0) through the entire interval. The spectra at midnight does not have a clear peak during the first period (0330–0404 UT), when the dipolarization is observed at geosynchronous. From 0404 to 0545 UT, the tail of the spectra gradually increases in slope, finally settling to a Maxwellian-like distribution during the final period (0511–0545 UT).

[15] In Figure 7, we present equatorial energy density (5–30 keV) profiles calculated from the deconvolved ion intensities for this interval. The peak in energy density of the ring current begins in the premidnight region during 0330–0404 UT and spreads out in MLT during 0404–0437 UT. By 0437–0511 UT, the peak in ring current energy density has decreased in magnitude and spatial extent slightly and now extends from midnight to dusk. The energy density continues to fall in the next time interval and peaks at midnight. The magnitude of the peak in the energy density between 5 and 30 keV does not increase with falling Sym-H
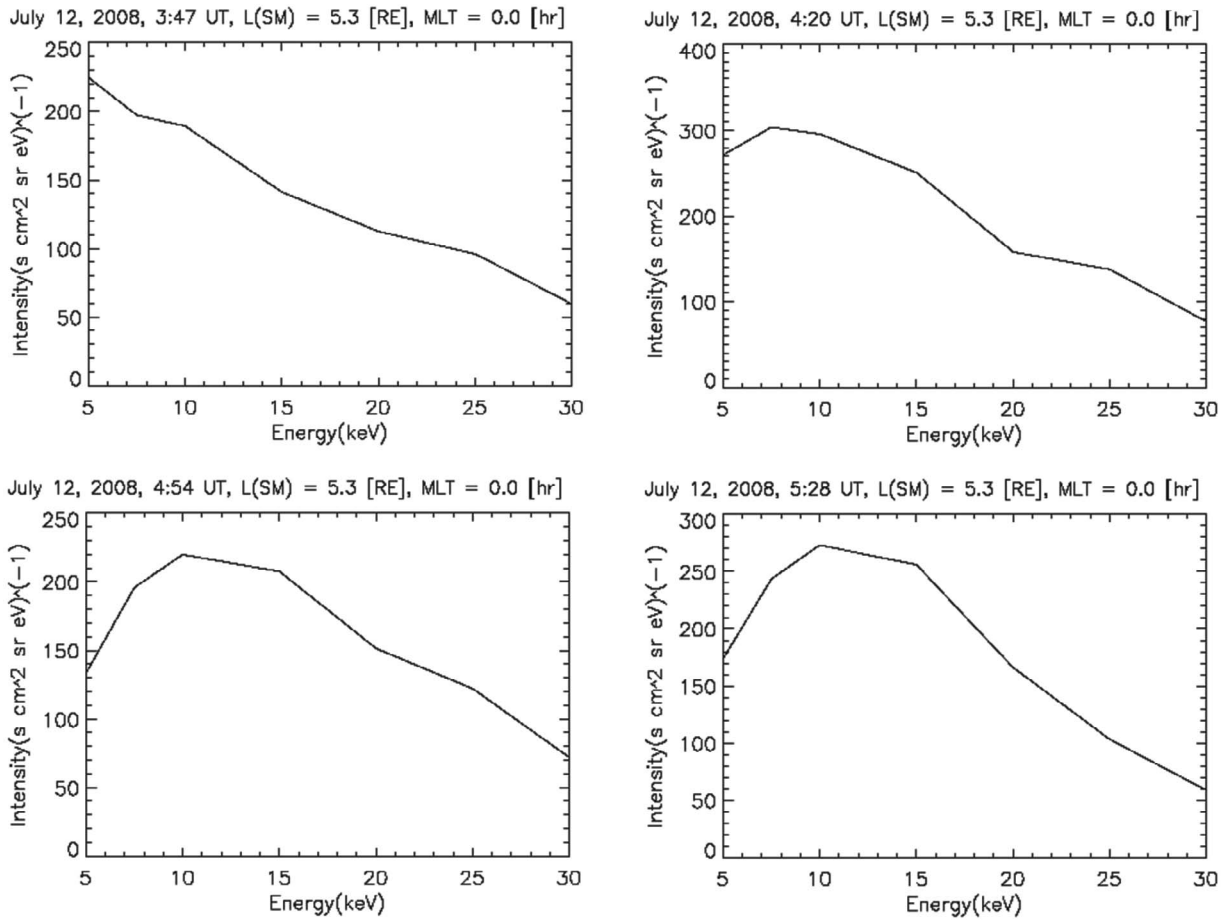
Figure 6. Evolution of intensity spectra at $R = 5.3$, MLT = 0.0 (0330–0545 UT) on 12 July 2008.

but rather rises and falls following dipolarization events observed at geosynchronous orbit.

2.2. The 10 August 2008 Event

[16] Five minute averages of IMF B_y, B_z, AE, and Sym-H provided by OMNI for the day of 10 August 2008 are presented in Figure 8 (left). Again, the vertical lines indicate the time interval observed by TWINS-1, and we zoom in on this interval using 1 min resolution OMNI data on the right. There are two large negative IMF B_y regions in the interval, the first occurring between 0520 and 0600 UT and the second between 0620 and 0730 UT. IMF B_y is also slightly negative for 15 min just after 0600 UT. IMF B_z is negative for most of the interval, with slight northerly excursions
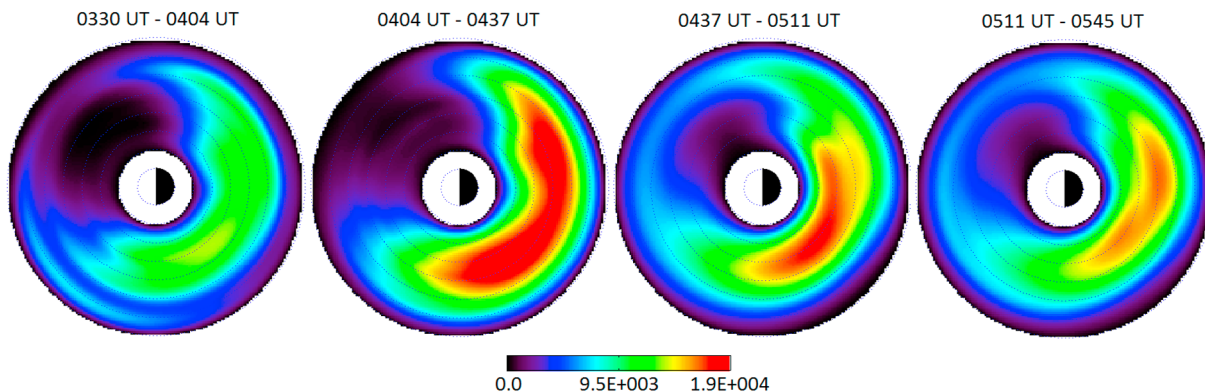
Figure 7. Equatorial 5–30 keV energy density profiles for 12 July 2008.
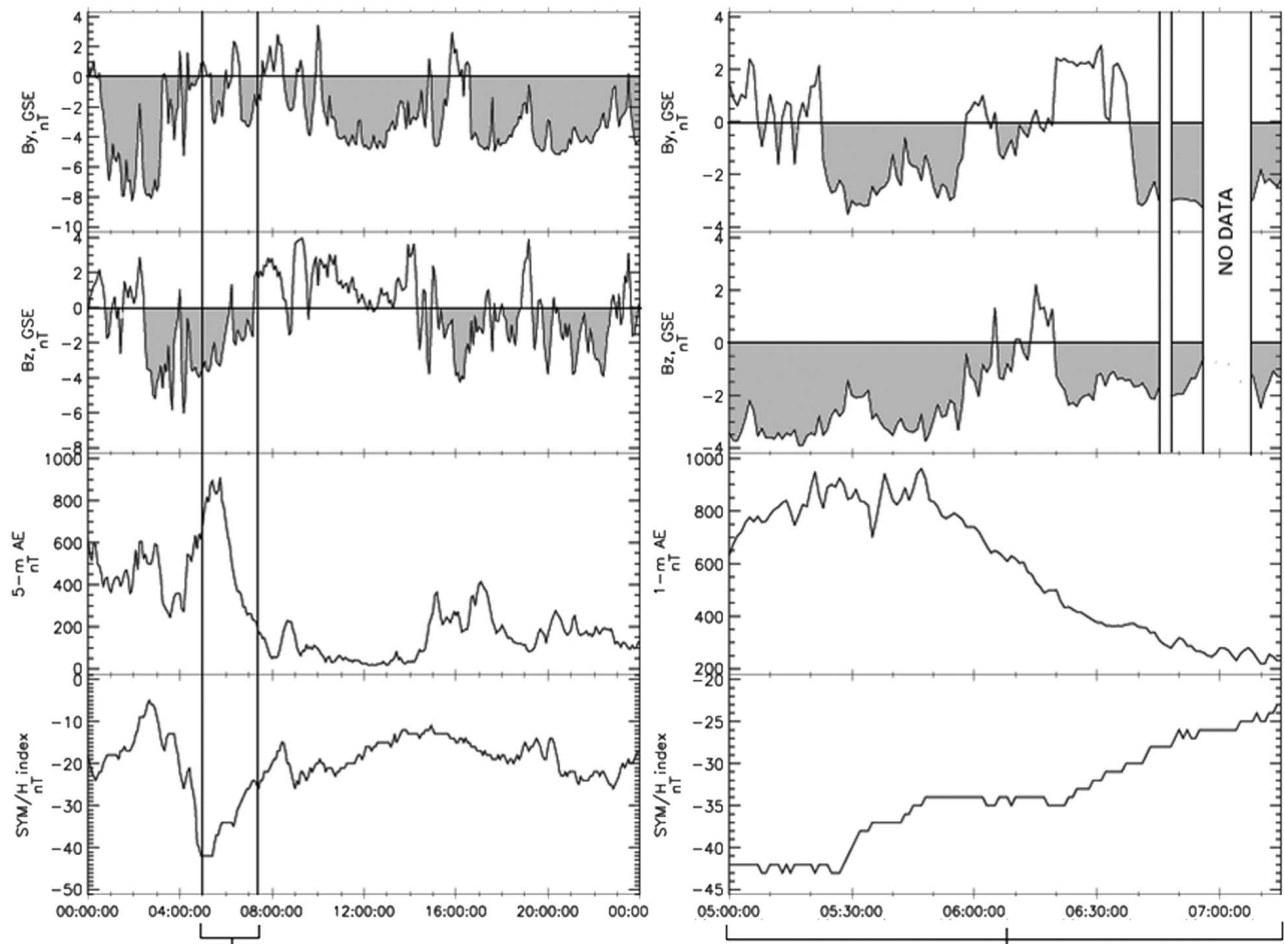
Figure 8. The IMF B_y, B_z, AE, and Sym-H indices for (left) 10 August 2008 and (right) 0500–0715 UT.

between 0600 and 0620 UT. AE peaks between 0520 and 0545 UT, reaching over 900 nT at times. AE then falls off to slightly above 200 nT before the end of the interval. Sym-H increases by 20 nT over the interval and is relatively flat during 0500–0530 and 0540–0620 UT. Both AE and Sym-H seem to be controlled by southward IMF B_z. Note that the time of interest is in the early recovery stage of the storm just after the minimum in Sym-H.

[17] The 10 keV ENA images for 0500–0715 UT are shown in Figure 9. Again, we use 24 sweep, 33 min averages projected onto a sky map, with the red and purple L shells indicating sunward and duskward directions. The TWINS-1 spacecraft is at $R = 7.1$ R_e, 65.6° latitude during 0500–0533 UT, viewing from dawn in the Northern Hemisphere. It progresses to $R = 6.7$ R_e, 62.8° latitude throughout the interval. During 0500–0533 UT, TWINS-1 observes the majority of 10 keV ENAs being produced as low-altitude emissions. The ENAs from low-altitude emissions peak during 0533–0607 UT and then fall off gradually until the end of the interval. We also observe a gradual increase in high-altitude emissions directly from ring current ions between midnight and dawn during 0500 and 0640 UT. The high-altitude emissions appear to drop off during the 0640–0715 UT interval.

[18] Figure 10 shows the geomagnetic field at geosynchronous orbit measured by GOES-12 (left) and GOES-11 (right) on 10 August 2008. The locations of the geosynchronous spacecraft are shown in Figure 11. GOES-11 observes a dipolarization signature at 0500 UT near dusk. GOES-12 observes a similar signature at 0530 UT just dawnward of midnight.

[19] As an example of the energy-dependent global images during this period, the 5–30 keV equatorial ion intensities for 0640–0715 UT are shown in Figure 12. We observe two peaks in the 10 keV ion intensity, one near midnight between $L = 3$ and $L = 5$ and one near dusk between $L = 6$ and $L = 7$. The spectra for these two peaks are shown in Figure 13. From the spectra, we observe that these two locations contain different plasma populations. The spectra at midnight peak at 10 keV, while the spectra near dusk peak at 15 keV.

[20] The 5–30 keV equatorial energy densities are shown in Figure 14. The energy density is initially peaked in the premidnight region between $L = 3$ and $L = 5$. During 0533–0606 UT, the energy density increases by a factor of 2 as a result of the plasma injection inferred from geosynchronous measurements. This evolves into two peaks during 0607–0640 UT, one near midnight between $L = 3$ and $L = 5$ and one
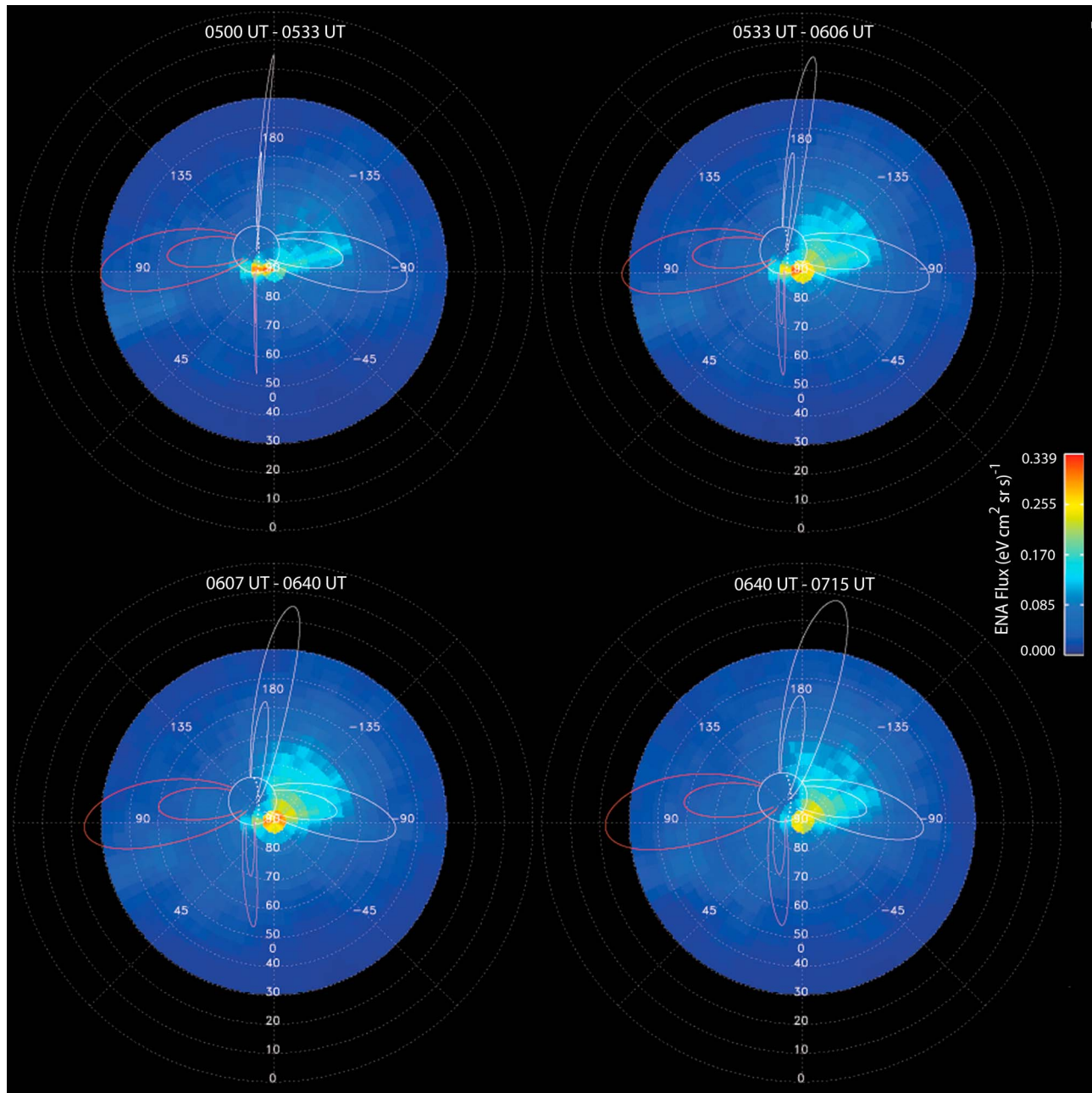
Figure 9. TWINS-1 10 keV ENA flux for 0500–0715 UT on 10 August 2008.

near dusk between $L = 6$ and $L = 7$. Both peaks then decrease in magnitude over the next hour while maintaining their spatial structure. Again, the strength of the energy density between 5 and 30 keV seems to follow dipolarization.

2.3. The 4 September 2008 Event

[21] Figure 15 (left) shows the IMF B_y and B_z, as well as the AE and Sym-H indices for the day of 4 September 2008. The time of interest is marked by vertical lines and expanded on the right using 1 min resolution OMNI data. IMF B_y is positive for the majority of the interval, with negative excursions at the beginning of the interval and from 0450 to 0520 UT. IMF B_z is negative for most of the interval

with a single northerly excursion at 0515 UT. The AE index is elevated for the entire interval but steadily decreases from 1400 nT at 0325 UT to 500 nT. Sym-H reaches −67 nT just before 0400 UT, making this the strongest storm studied in this paper. Note that the time of interest is again in the early recovery phase of the storm.

[22] The geomagnetic field measured by Geotail in the plasma sheet ($x \sim -17 \ R_e$) is shown in Figure 16 (left). The ion number density and ion bulk flow velocity measured by the Solar Wind Analyzer (SWA) instrument are shown on the right of Figure 16. A bursty bulk flow (BBF) [Angelopoulos et al., 1994] is identified at 0418 UT by the large earthward V_x component of the ion bulk flow velocity
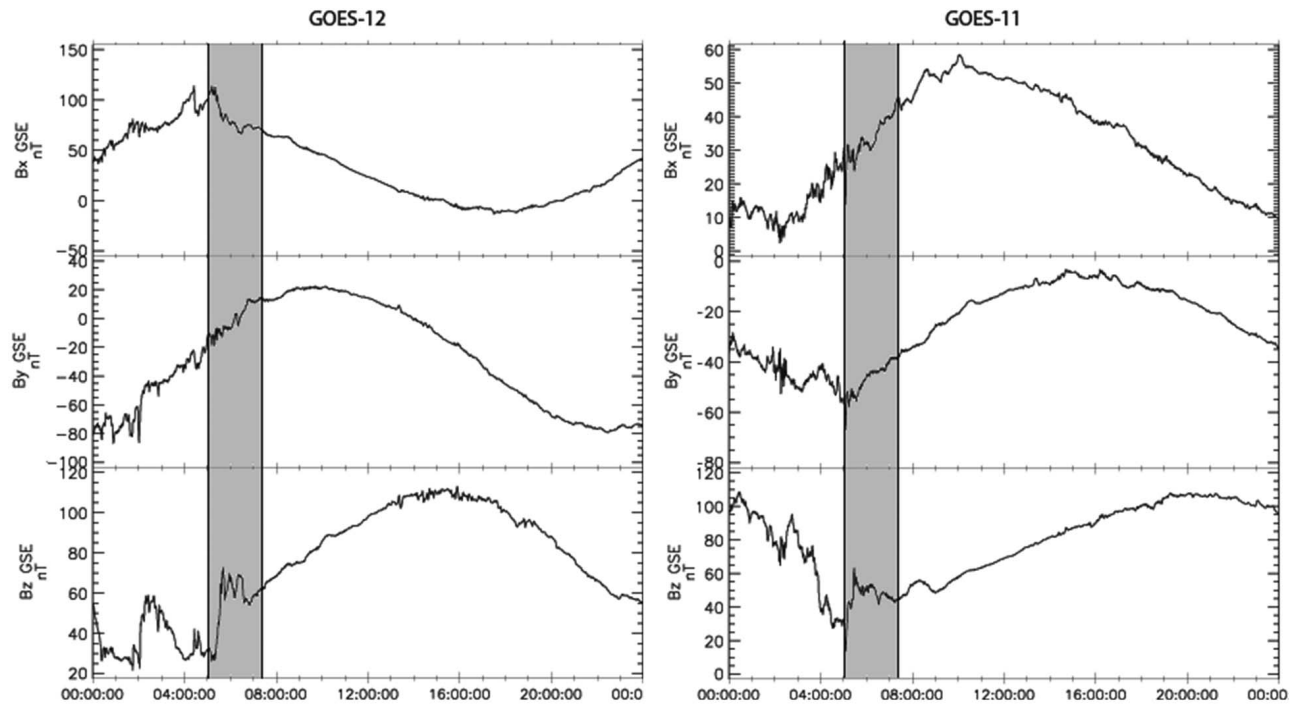
Figure 10. (left) GOES-12 and (right) GOES-11 geomagnetic field data for 10 August 2008.

and the positive turn in B_z. The large B_x component of the geomagnetic field measured by Geotail prior to the injection shows the field stretching until the dipolarization is observed. Figure 17 shows the geomagnetic field at geosynchronous orbit measured by GOES-12 (left) and GOES-11 (right). The GOES spacecraft locations for this interval are shown in Figure 18. Both GOES spacecraft see the dipolarization just prior to 0430 UT.

[23] The 10 keV ENA images from TWINS-1 for 0313–0527 UT are shown in Figure 19. TWINS-1 is near apogee ($R = 7.12$ R_e), viewing from dawn at the beginning of the observations. Low-altitude emissions are clearly visible throughout the entire interval. They first peak during 0313–0346 UT, drop off during 0346 UT, come back during 0420–0454 UT, and then drop off again. High-altitude emissions from dawn to midnight are also visible at all times and gradually increase from 0420–0454 to 0454–0527 UT.

[24] As an example of the energy-dependent global images during this period, the deconvolved equatorial ion intensities for 5–30 keV ions during 0347–0420 UT are shown in Figure 20. Prior to the plasma injection, a single peak is observed at midnight between $L = 3$ and $L = 5$.

[25] Figure 21 shows the evolution of the energy spectrum in the peak at midnight throughout the entire time period (0313–0527 UT). The peak in ion intensity appears to be at an energy higher than 30.0 keV both prior to and after the injection. We compare the ENA intensity calculated from the result of the inversion to the measured ENA intensity for 0454–0527 UT in Figure 22 (10 keV) and Figure 23 (20 keV). The bright emissions from the outer pixels beneath the sunline in the measured intensity are due to instrumental effects and are not reproduced by the deconvolved ion intensity. The ENA intensity calculated from the ion distribution produces the same overall features as in the measured ENA intensity, indicating that the ion distribution

the inversion technique produces well explain the measured ENA intensity.

[26] The equatorial energy densities calculated from the deconvolved ion distribution for the entire interval are shown in Figure 24. The energy density in the ring current peaks slightly duskward of midnight during 0313–0420 UT. It then increases in two locations, one between $L = 3$ and $L = 5$, which is still slightly in the postmidnight region, and one at $L = 6$, with its peak reaching from dusk to midnight. The energy density in the ring current then drops off again during 0454–0527 UT. The peak at midnight remains in the same location, while the peak between dusk to midnight has disappeared. The strength of the energy density between 5 and 30 keV appears to be driven by an injection associated with a dipolarization observed at geosynchronous and deeper in the tail rather than following Sym-H.

3. Discussion and Summary

[27] One important aspect of analyzing the ENA images presented in the previous section is in understanding the
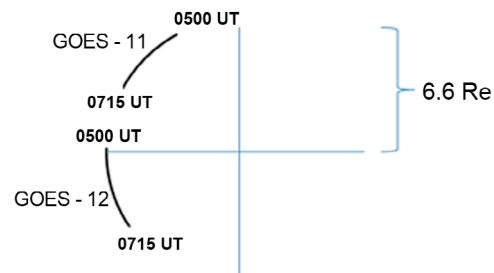

**Figure 11.** GOES equatorial spacecraft locations for 0500–0715 UT on 10 August 2008.
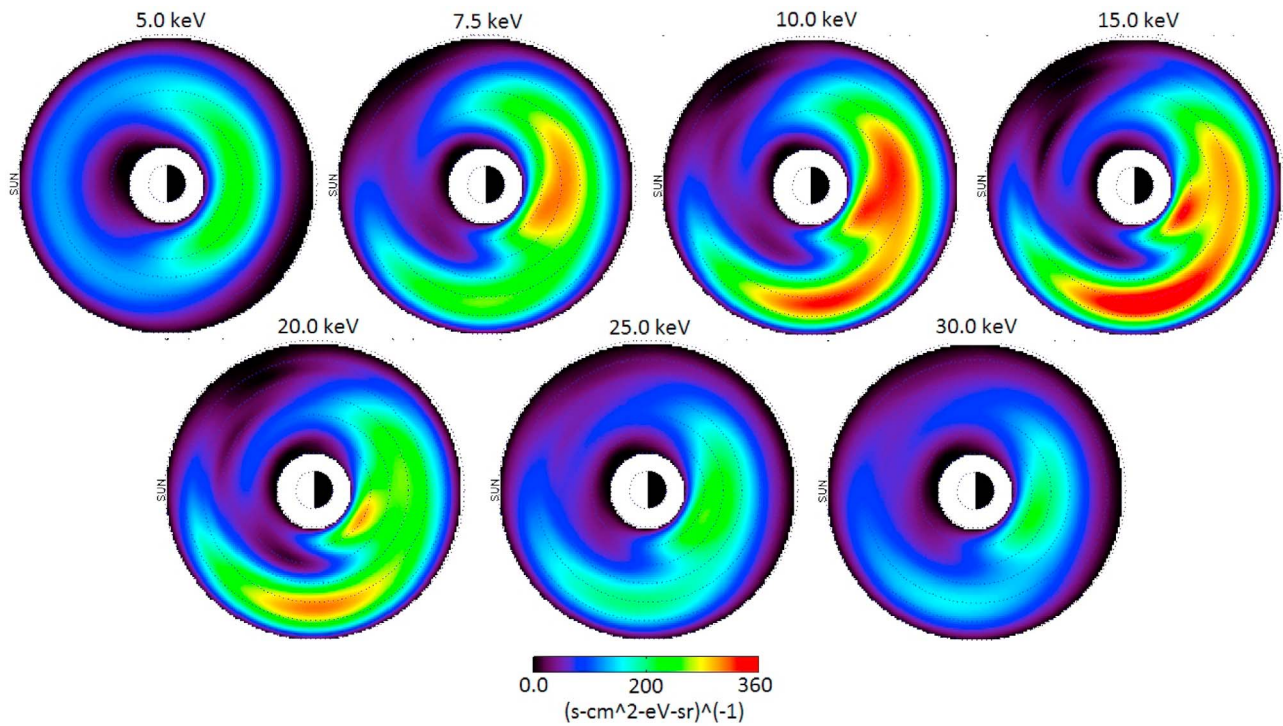
Figure 12. Equatorial intensity averaged over pitch angle for 5–30 keV ions on 10 August 2008, 0640–0715 UT.

impact of geocoronal density at different altitudes. Because of the higher geocoronal density at low altitudes, precipitating particles tend to dominate the ENA emissions. These low-altitude emissions typically belong to a ring current plasma population on the opposite side of Earth and are viewed just off Earth's limb [*Roelof*, 1987; *Bazell et al.*, 2010]. These emissions are clear in Figures 2, 9, and 19. It should be noted that the link between sources in the ring current intensity and the low-altitude emissions depends upon the use of the thick target approximation and the

magnetic field mapping. The higher-energy density in the premidnight sector shown in Figure 7 is believed to be the source of the precipitating particles creating the low-altitude emissions seen off the Earth's limb in Figure 2. Note that the low-altitude emissions are observed from both hemispheres throughout 0330–0511 UT. The low-altitude emissions in Figure 9 are also clearly observed just off the Earth's limb. These are believed to originate from the duskward peak in ring current energy density in Figure 14. We observe low-altitude emissions emanating from both hemispheres again
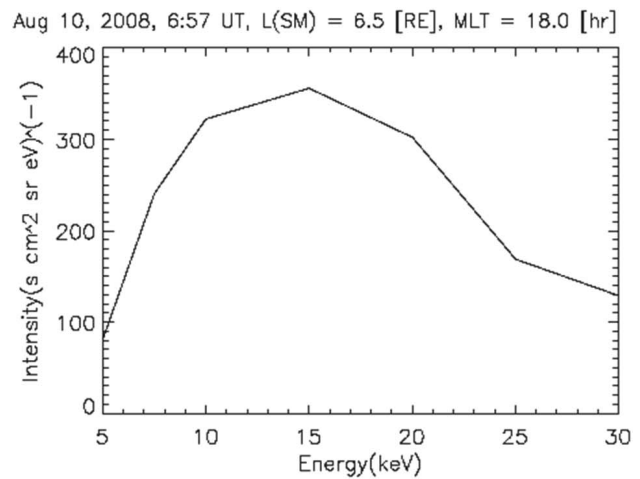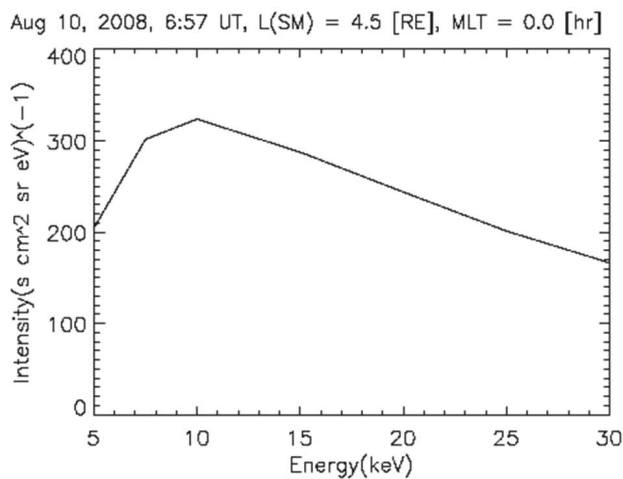
Figure 13. The 10 August 2008, 0640–0715 UT (a) 5–30 keV intensity spectra at $R = 4.5$, MLT = 0.0 and (b) $R = 6.5$, MLT = 18.
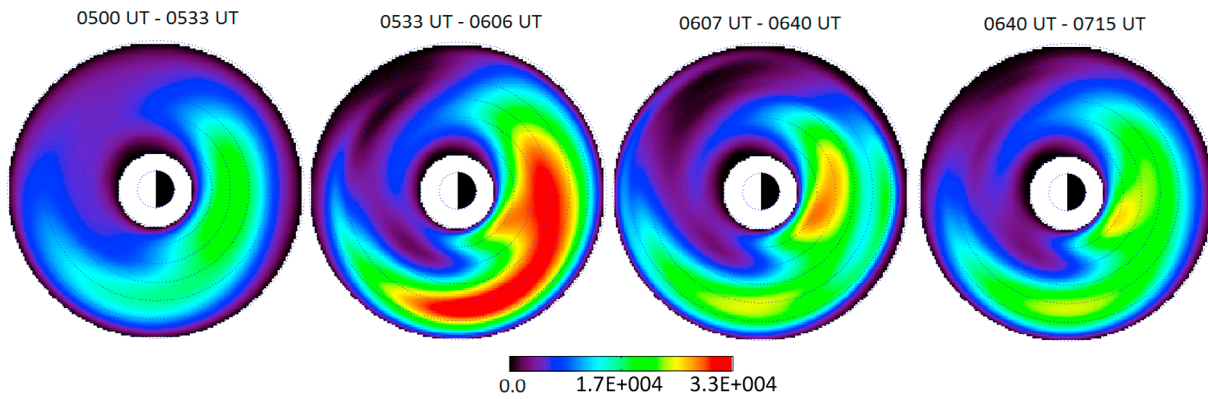
Figure 14. The 5–30 keV equatorial energy density profiles for 0500–0715UT on 10 August 2008.

for the 4 September storm in Figure 19. Again, these are believed to have their sources in the duskward peak in energy density in Figure 24. For each case, ENA intensity increases after the dipolarization signature is seen at geosynchronous, which is consistent with previous observations by *Lui et al.* [2001] and *Ohtani et al.* [2005].

[28] Dipolarization signatures are observed near minimum Sym-H for both the August and September 2008 events,

which is consistent with previous geosynchronous observations [*Iyemori and Rao*, 1996; *Ohtani et al.*, 2001]. The immediate increase in Sym-H following the substorm injection is believed to be due to a reduction of the cross-tail current [*Siscoe and Petschek*, 1997]. We find that just after a plasma injection there are often two peaks in the 5–30 keV ring current plasma energy density, one near midnight between $L = 3$ and $L = 5$ and one between dusk and midnight
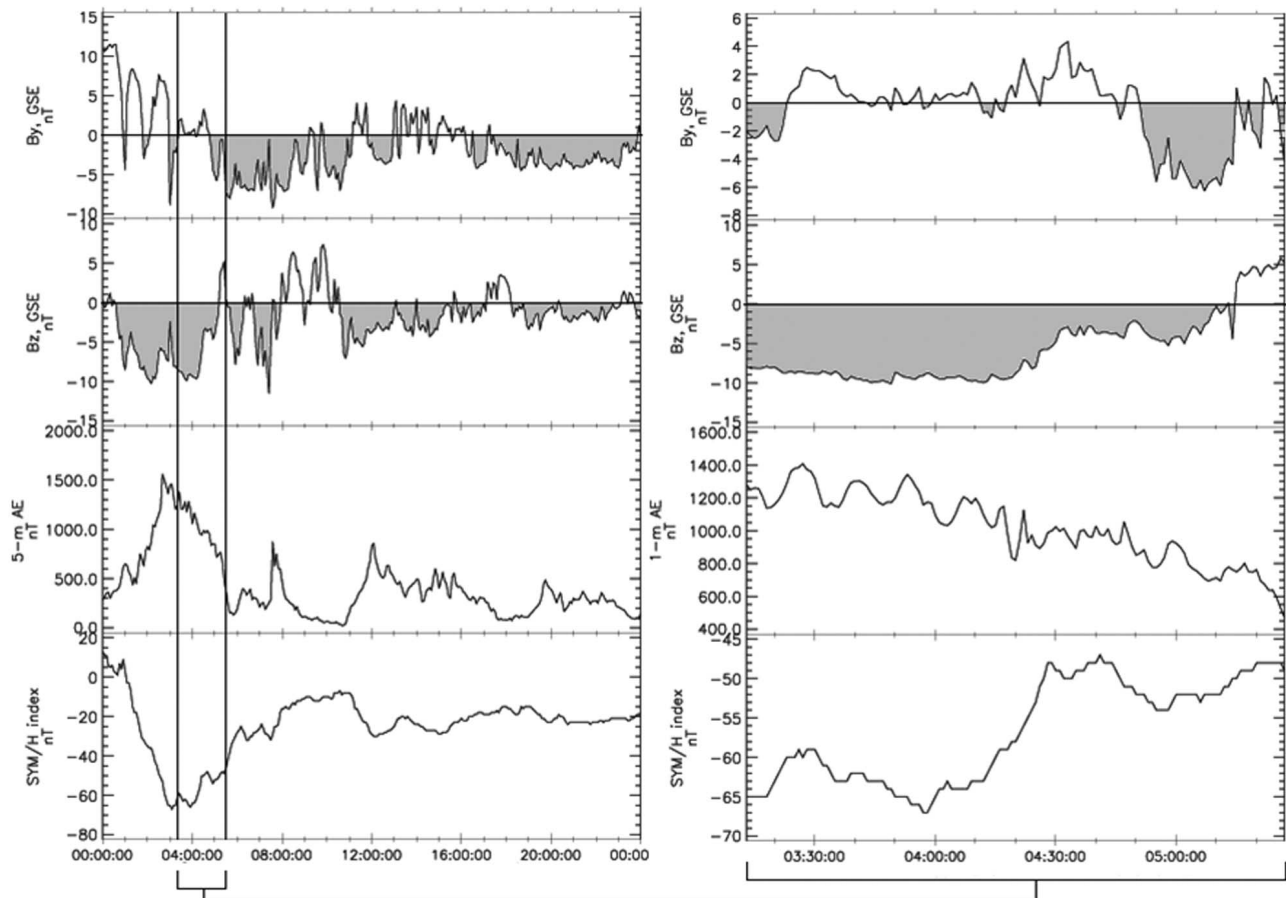

Figure 15. The IMF B_y, B_z, AE, and Sym-H indices for (left) 4 September 2008 and (right) 0313–0527 UT.
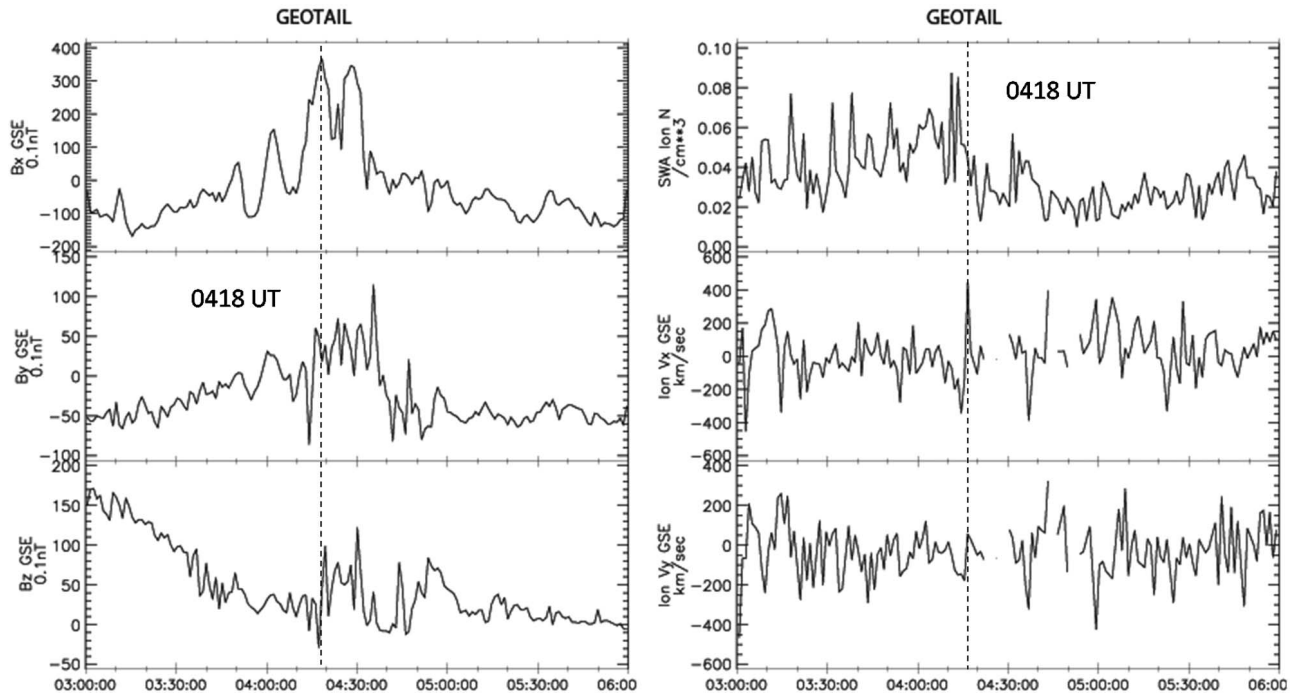
Figure 16. Geotail (left) geomagnetic field data and (right) ion density, V_x and V_y, for 0300–0600 UT on 4 September 2008. The dashed vertical line indicates the dipolarization and plasma injection at 0418 UT.

between $L = 5$ and $L = 7$. The peak in 5–30 keV energy density tends to be located primarily in the premidnight region, which is consistent with the in situ observations of the ring current shown by *Le et al.* [2004] and *Lui* [2003], as well as the in situ geosynchronous MPA observations [*Korth et al.*, 1999; *Denton et al.*, 2005; *Zhang et al.*, 2006] and

simulations of plasma pressure in the ring current [*Zhang et al.*, 2007]. We do not observe the extreme dawnward peaks in equatorial ion intensity that *Brandt et al.* [2002] shows, but this is believed to be due to the different driving mechanisms in the solar wind. *Brandt et al.* [2002] studies an
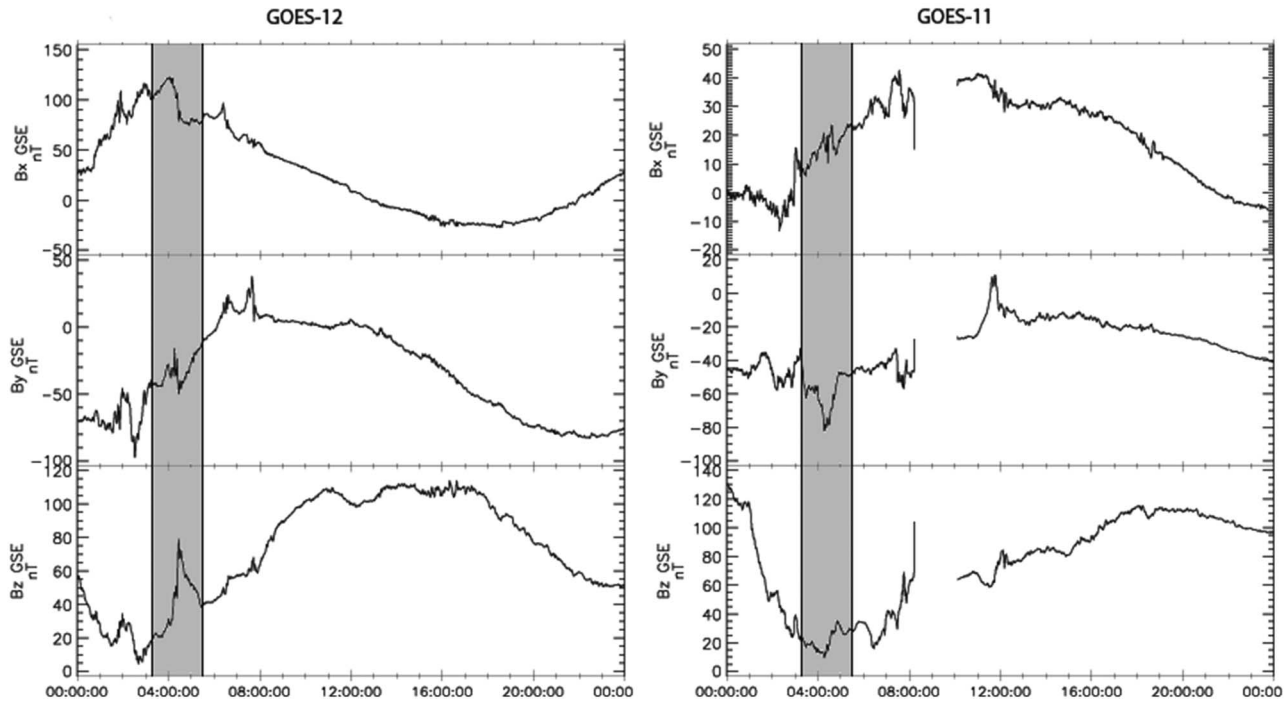
Figure 17. (left) GOES-12 and (right) GOES-11 geomagnetic field data for 4 September 2008.
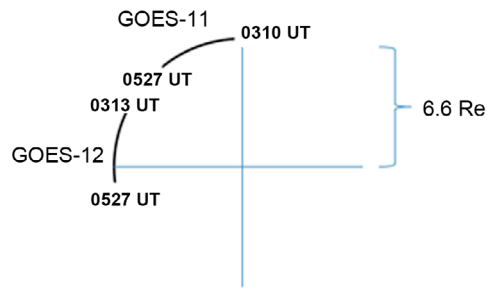
Figure 18. GOES equatorial spacecraft locations for 0313–0527 UT on 4 September 2008.

ICME-driven storm, while the present study investigates much weaker, CIR-driven storms.

[29] To summarize, we have shown global images of trapped ring current particles with energies between 5 and 30 keV during the main phase and early recovery phase of CIR-driven storms. We also have shown the energy spectra as a function of time. Of particular interest is the fact that during the early recovery phase of the strongest CIR-driven storm, where Sym-H dips below −65 nT and AE is greater than 1000 nT, the peak of the ion intensity in the ring current is greater than 30 keV. On the other hand, during the main and early recovery phases of the smaller storms, the peak of the ion intensity is around 10–15 keV. These
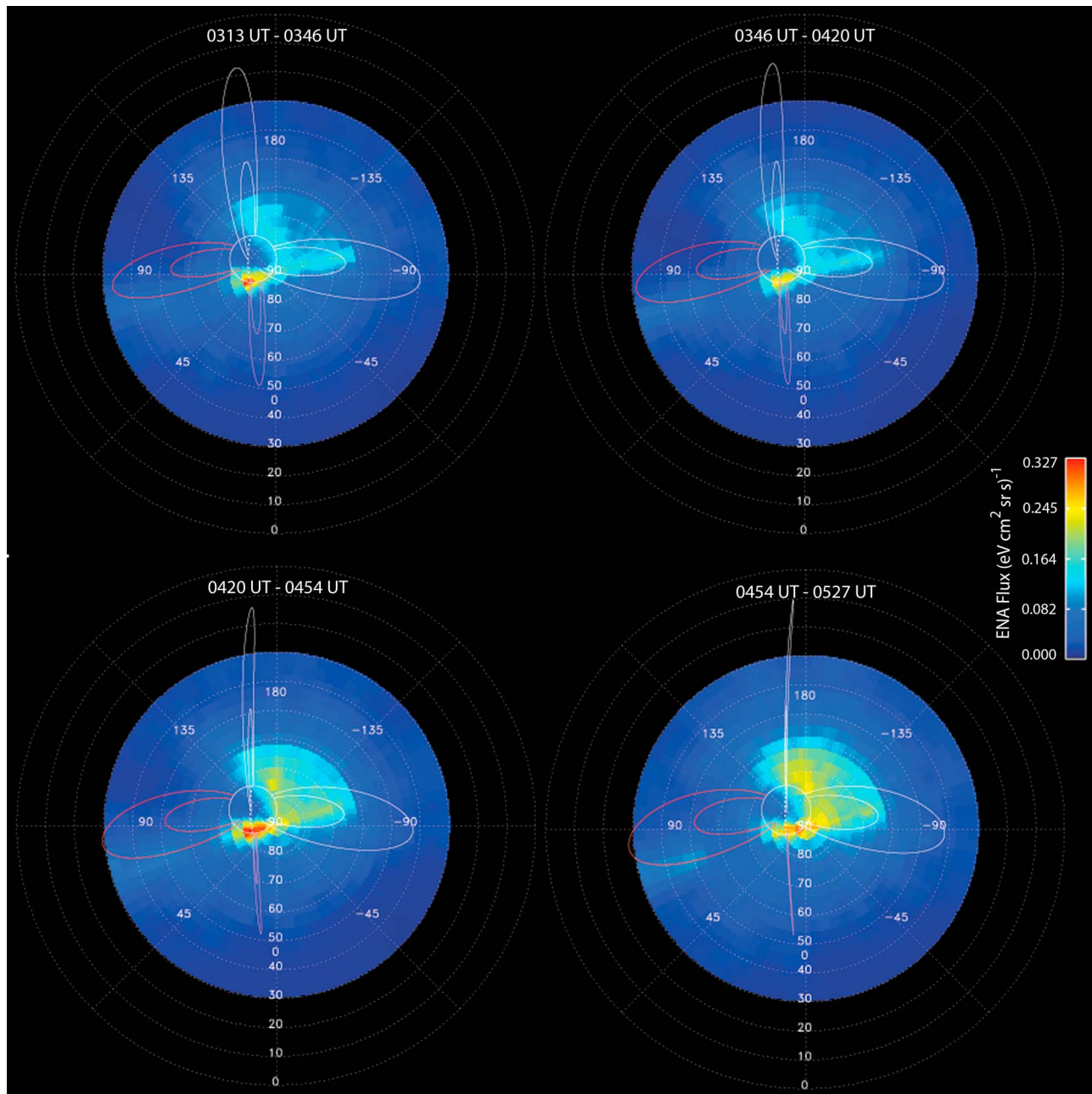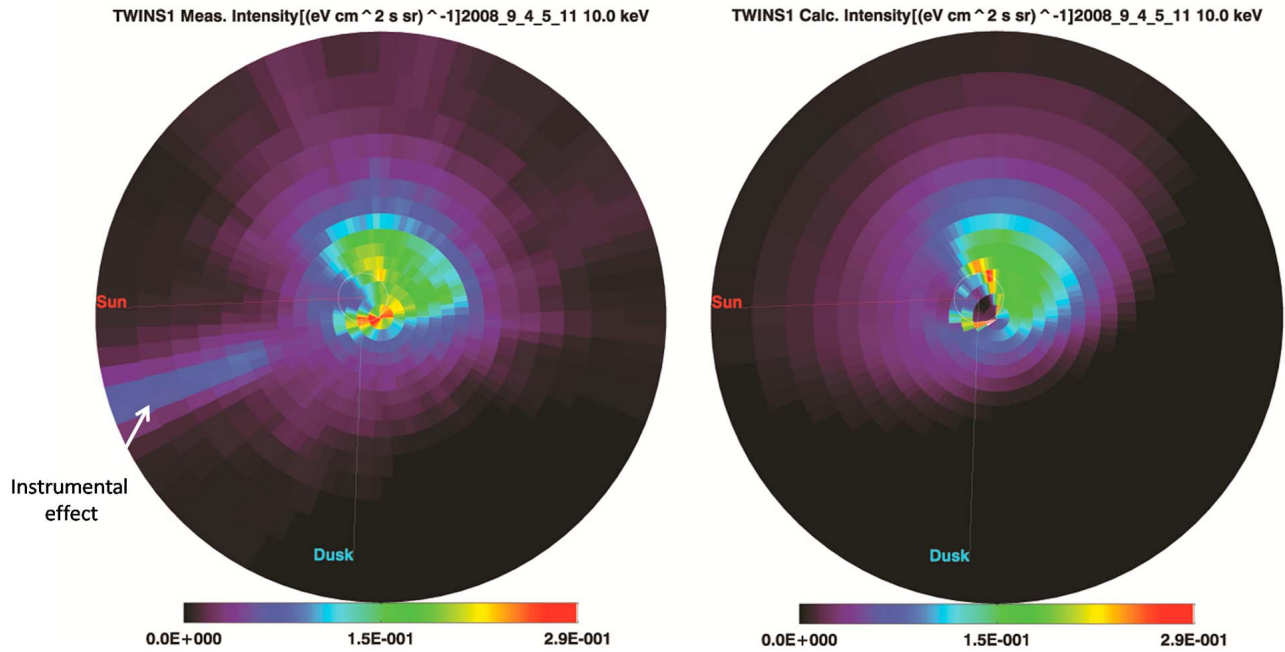

Figure 19. TWINS-1 10 keV ENA flux for 0313–0527 UT on 4 September 2008.
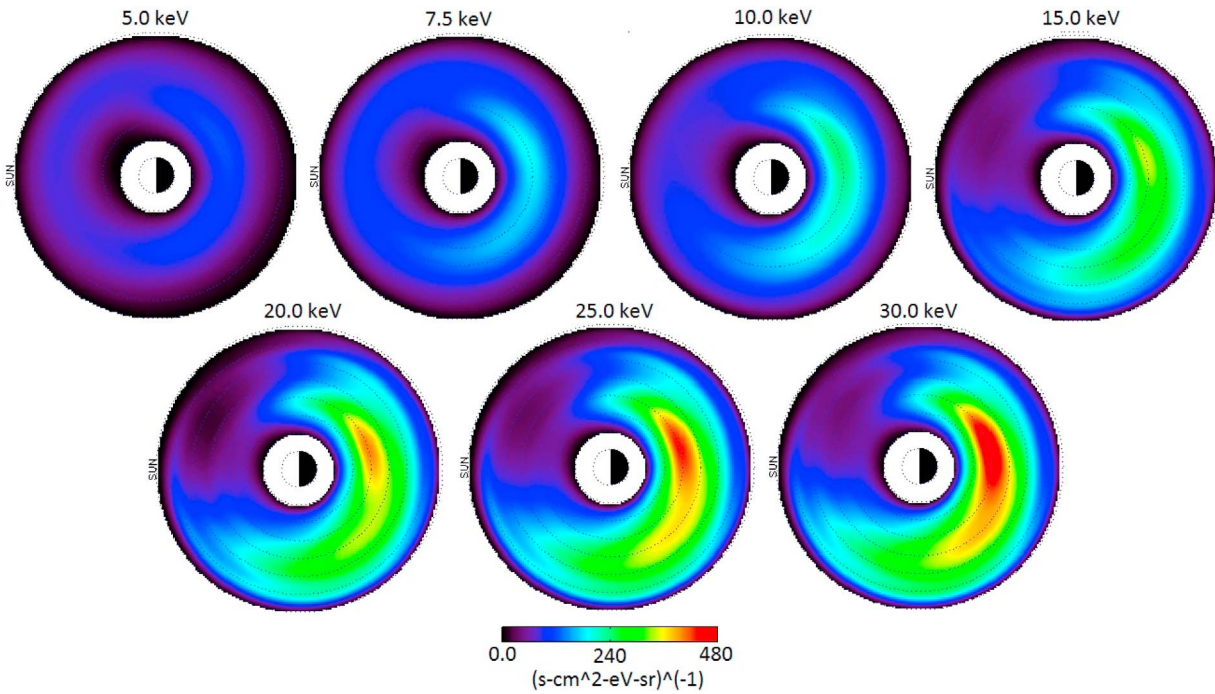
Figure 20. Equatorial intensity averaged over pitch angle for 5–30 keV ions on 4 September 2008, 0347–0420 UT.
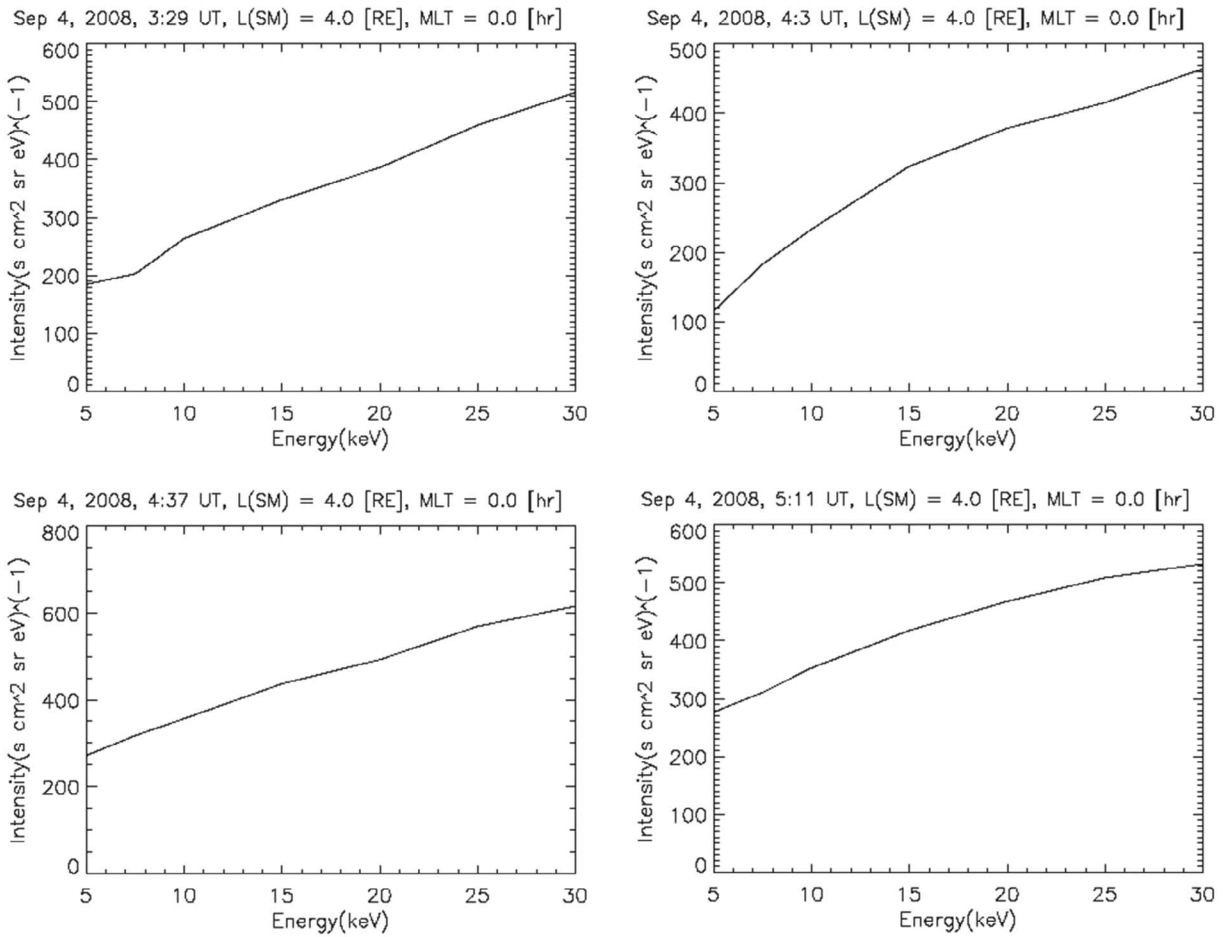
Figure 21. Evolution of 5–30 keV ion intensity spectra at $L = 4$, MLT = 0.0 on 4 September 2008, 0313 UT–0527 UT.
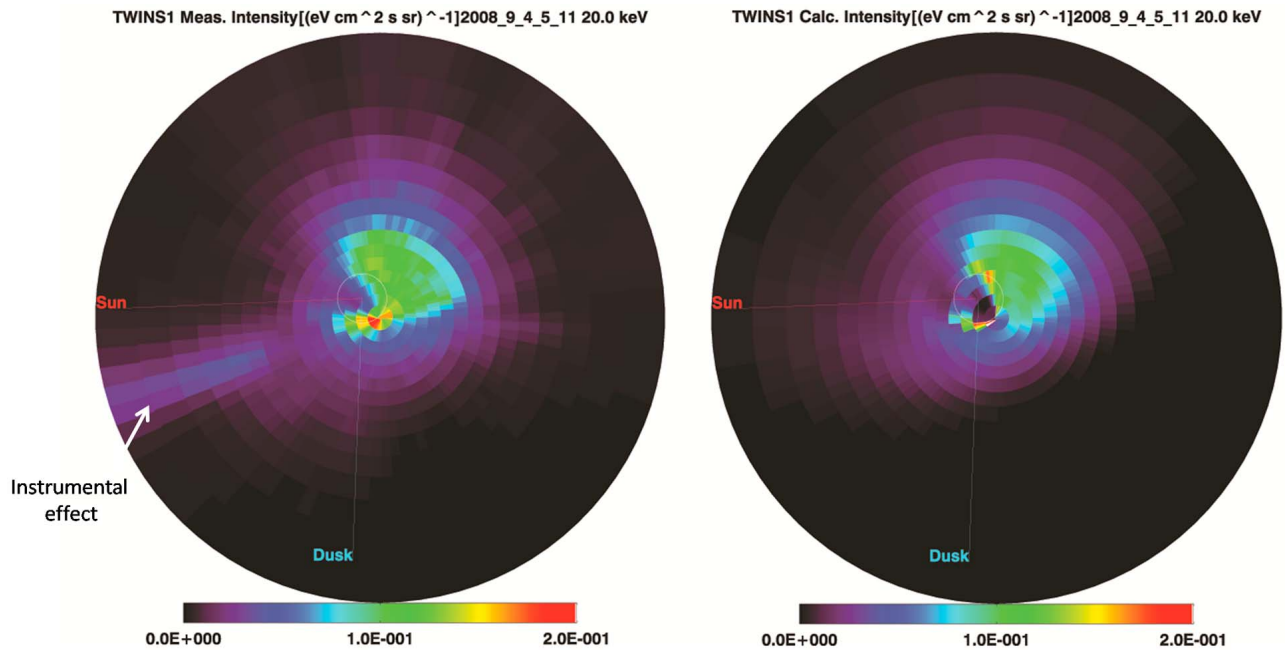
Figure 22. The 10 keV (left) measured ENA intensity and (right) calculated ENA intensity for 0454–0527 UT on 4 September 2008.

relationships between the storm conditions (both interplanetary and magnetospheric) and the ring current energy density do not appear to be casual, and detailed modeling analysis is needed to further understand the specifics of the spatial distribution and the energy spectra in context of the storm conditions. However, all three events used in this study show that the energy density of 5–30 keV ions in the ring current does not follow Sym-H but rather is directly and significantly enhanced by injections during both the main and early recovery phases of CIR-driven geomagnetic storms.
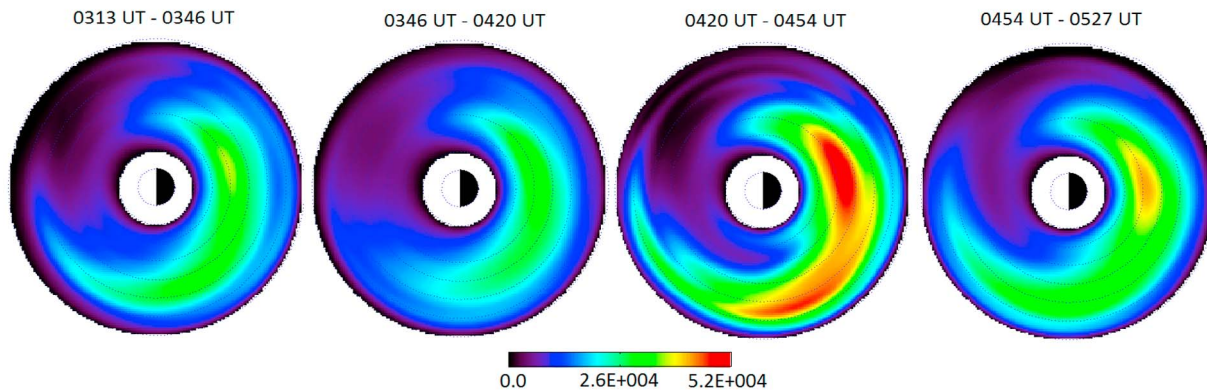
Figure 23. The 20 keV (left) measured ENA intensity and (right) calculated ENA intensity for 0454–0527 UT on 4 September 2008.

Figure 24. The 5–30 keV equatorial energy density profiles for 0313–0527 UT on 4 September 2008.

References

Angelopoulos, V., C. Kennel, F. Coroniti, R. Pellat, M. Kivelson, R. Walker, C. Russell, W. Baumjohann, W. Feldman, and J. Gosling (1994), Statistical characteristics of bursty bulk flow events, *J. Geophys. Res.*, *99*(A11), 21,257–21,280, doi:10.1029/94JA01263.

Bazell, D., E. C. Roelof, T. Sotirelis, P. C. Brandt, H. Nair, P. Valek, J. Goldstein, and D. McComas (2010), Comparison of TWINS images of low-altitude emission of energetic neutral atoms with DMSP precipitating ion fluxes, *J. Geophys. Res.*, *115*, A10204, doi:10.1029/2010JA015644.

Borovsky, J. E., and M. H. Denton (2006), Differences between CME-driven storms and CIR-driven storms, *J. Geophys. Res.*, *111*, A07S08, doi:10.1029/2005JA011447.

Brandt, P. C., S. Ohtani, D. G. Mitchell, M.-C. Fok, E. C. Roelof, and R. Demajistre (2002), Global ENA observations of the storm mainphase ring current: Implications for skewed electric fields in the inner magnetosphere, *Geophys. Res. Lett.*, *29*(20), 1954, doi:10.1029/2002GL015160.

Buzulukova, N., M.-C. Fok, J. Goldstein, P. Valek, D. J. McComas, and P. C. Brandt (2010), Ring current dynamics in moderate and strong storms: Comparative analysis of TWINS and IMAGE/HENA data with CRCM, *J. Geophys. Res.*, doi:10.1029/2010JA015292, in press.

Denton, M. H., M. F. Thomsen, H. Korth, S. Lynch, J. C. Zhang, and M. W. Liemohn (2005), Bulk plasma properties at geosynchronous orbit, *J. Geophys. Res.*, *110*, A07223, doi:10.1029/2004JA010861.

Denton, M. H., J. E. Borovsky, R. M. Skoug, M. F. Thomsen, B. Lavraud, M. G. Henderson, R. L. McPherron, J. C. Zhang, and M. W. Liemohn (2006), Geomagnetic storms driven by ICME- and CIR-dominated solar wind, *J. Geophys. Res.*, *111*, A07S07, doi:10.1029/2005JA011436.

Ebihara, Y., and M.-C. Fok (2004), Postmidnight storm time enhancement of tens-of-keV proton flux, *J. Geophys. Res.*, *109*, A12209, doi:10.1029/2004JA010523.

Ejiri, M., R. A. Hoffman, and P. H. Smith (1980), Energetic particle penetrations into the inner magnetosphere, *J. Geophys. Res.*, *85*(A2), 653–663, doi:10.1029/JA085iA02p00653.

Fok, M.-C., T. E. Moore, and M. E. Greenspan (1996), Ring current development during storm main phase, *J. Geophys. Res.*, *101*(A7), 15,311–15,322, doi:10.1029/96JA01274.

Gonzalez, W. D., J. A. Joselyn, Y. Kamide, H. W. Kroehl, G. Rostoker, B. T. Tsurutani, and V. M. Vasyliunas (1994), What is a geomagnetic storm?, *J. Geophys. Res.*, *99*(A4), 5771–5792, doi:10.1029/93JA02867.

Iyemori, T., and D. R. K. Rao (1996), Decay of the Dst field of geomagnetic disturbances after substorm onset and its implication to substorm relation, *Ann. Geophys.*, *14*, 608.

Kistler, L. M., and D. J. Larson (2000), Testing electric and magnetic field models of the storm time inner magnetosphere, *J. Geophys. Res.*, *105*(A11), 25,221–25,231, doi:10.1029/2000JA000132.

Korth, H., M. F. Thomsen, J. E. Borovsky, and D. J. McComas (1999), Plasma sheet access to geosynchronous orbit, *J. Geophys. Res.*, *104*(A11), 25,047–25,061, doi:10.1029/1999JA900292.

Krieger, A. S., A. F. Timothy, and E. C. Roelof (1973), A coronal hole and its identification as the source of a high velocity solar wind stream, *Sol. Phys.*, *23*, 123.

Le, G., C. Russell, and K. Takahashi (2004), Morphology of the ring current derived from magnetic field observations, *Ann. Geophys.*, *22*, 1267–1295.

Lui, A. T. Y., R. W. McEntire, M. Nosé, and D. J. Williams (2001), Composition of energetic neutral atoms during a storm main phase, *Geophys. Res. Lett.*, *28*(7), 1363–1366, doi:10.1029/2000GL012612.

Lui, A. T. Y. (2003), Inner magnetospheric plasma pressure distribution and its local time asymmetry, *Geophys. Res. Lett.*, *30*(16), 1846, doi:10.1029/2003GL017596.

McComas, D. J., et al. (2009a), The Two Wide-Angle Imaging Neutral-Atom Spectrometers (TWINS) NASA mission-of-opportunity, *Space Sci. Rev.*, *142*, 157–231, doi:10.1007/s11214-008-9467-4.

McComas, D. J., et al. (2009b), Global observations of the interstellar interaction from the Interstellar Boundary Explorer (IBEX), *Science*, *326*, 959–962, doi:10.1126/science.1180906.

Ohtani, S., M. Nosé, G. Rostoker, H. Singer, A. T. Y. Lui, and M. Nakamura (2001), Storm-substorm relationship: Contribution of the tail current to Dst, *J. Geophys. Res.*, *106*, 21,199–21,209, doi:10.1029/2000JA000400.

Ohtani, S., P. C. Brandt, D. G. Mitchell, H. Singer, M. Nosé, G. D. Reeves, and S. B. Mende (2005), Storm-substorm relationship: Variations of the hydrogen and oxygen energetic neutral atom intensities during storm time substorms, *J. Geophys. Res.*, *110*, A07219, doi:10.1029/2004JA010954.

Roelof, E. C. (1987), Energetic neutral atom image of a storm-time ring current, *Geophys. Res. Lett.*, *14*(6), 652–655, doi:10.1029/GL014i006p00652.

Sandanger, M. I., F. Soraas, K. Aarsnes, K. Oksavik, D. S. Evans, and M. S. Greer (2005), Proton injections into the ring current associated with B_z variations during HILDCAA events, in *The Inner Magnetosphere: Physics and Modeling, Geophys. Monogr. Ser.*, vol. 155, edited by T. I. Pulkkinen, N. A. Tsyganenko, and R. H. W. Friedel, p. 2249, AGU, Washington, D. C.

Siscoe, G. L., and H. E. Petschek (1997), On storm weakening during substorm expansion phase, *Ann. Geophys.*, *15*, 211.

Stüdemann, W., et al. (1987), The May 2–3, 1986 magnetic storm: First energetic ion composition observations with the Mics instrument on Viking, *Geophys. Res. Lett.*, *14*(4), 455–458, doi:10.1029/GL014i004p00455.

Tsurutani, B., and W. Gonzalez (1987), The cause of high-intensity long duration continuous AE activity (HILDCAAs): Interplanetary Alfven wave trains, *Planet. Space Sci.*, *35*, 405–412.

Tsurutani, B. T., et al. (2006), Corotating solar wind streams and recurrent geomagnetic activity: A review, *J. Geophys. Res.*, *111*, A07S01, doi:10.1029/2005JA011273.

Wahba, G. (1990), *Spline Models for Observational Data*, Soc. Industrial Appl. Math., Phil.

Zhang, J.-C., M. W. Liemohn, M. F. Thomsen, J. U. Kozyra, M. H. Denton, and J. E. Borovsky (2006), A statistical comparison of hot-ion properties at geosynchronous orbit during intense and moderate geomagnetic storms at solar maximum and minimum, *J. Geophys. Res.*, *111*, A07206, doi:10.1029/2005JA011559.

Zhang, J., et al. (2007), Understanding storm time ring current development through data model comparisons of a moderate storm, *J. Geophys. Res.*, *112*, A04208, doi:10.1029/2006JA011846.

J. Goldstein, D. J. McComas, and P. Valek, Southwest Research Institute, San Antonio, TX 78249, USA.

E. W. Grimes and J. D. Perez, Physics Department, Auburn University, Auburn, AL 36839, USA. (eric@auburn.edu)